



Average cosine coefficient and spectral distribution of the light field under sea ice: Implications for primary production

L. Matthes, J. Ehn, S. L.-Girard, N. Pogorzelec, M. Babin, C. Mundy

► To cite this version:

L. Matthes, J. Ehn, S. L.-Girard, N. Pogorzelec, M. Babin, et al.. Average cosine coefficient and spectral distribution of the light field under sea ice: Implications for primary production. *Elementa: Science of the Anthropocene*, 2019, 7 (1), pp.25. 10.1525/elementa.363 . hal-02415055

HAL Id: hal-02415055

<https://hal.science/hal-02415055>

Submitted on 10 Apr 2022

HAL is a multi-disciplinary open access archive for the deposit and dissemination of scientific research documents, whether they are published or not. The documents may come from teaching and research institutions in France or abroad, or from public or private research centers.

L'archive ouverte pluridisciplinaire **HAL**, est destinée au dépôt et à la diffusion de documents scientifiques de niveau recherche, publiés ou non, émanant des établissements d'enseignement et de recherche français ou étrangers, des laboratoires publics ou privés.



Distributed under a Creative Commons Attribution 4.0 International License

RESEARCH ARTICLE

Average cosine coefficient and spectral distribution of the light field under sea ice: Implications for primary production

L. C. Matthes*, J. K. Ehn*, S. L.-Girard†, N. M. Pogorzelec*, M. Babin† and C. J. Mundy*

The Arctic spring phytoplankton bloom has been reported to commence under a melting sea ice cover as transmission of photosynthetically active radiation (PAR; 400–700 nm) suddenly increases with the formation of surface melt ponds. Spatial variability in ice surface characteristics, i.e., snow thickness or melt pond distributions, and subsequent impact on transmitted PAR makes estimating light-limited primary production difficult during this time of year. Added to this difficulty is the interpretation of data from various sensor types, including hyperspectral, multispectral, and PAR-band irradiance sensors, with either cosine-corrected (planar) or spherical (scalar) sensor heads. To quantify the impact of the heterogeneous radiation field under sea ice, spectral irradiance profiles were collected beneath landfast sea ice during the Green Edge ice-camp campaigns in May–June 2015 and June–July 2016. Differences between PAR measurements are described using the downwelling average cosine, μ_d , a measure of the degree of anisotropy of the downwelling underwater radiation field which, in practice, can be used to convert between downwelling scalar, E_{od} , and planar, E_d , irradiance. A significantly smaller μ_d (PAR) was measured prior to snow melt compared to after (0.6 vs. 0.7) when melt ponds covered the ice surface. The impact of the average cosine on primary production estimates, shown in the calculation of depth-integrated daily production, was 16% larger under light-limiting conditions when E_{od} was used instead of E_d . Under light-saturating conditions, daily production was only 3% larger. Conversion of underwater irradiance data also plays a role in the ratio of total quanta to total energy (E_Q/E_w found to be 4.25), which reflects the spectral shape of the under-ice light field. We use these observations to provide factors for converting irradiance measurements between irradiance detector types and units as a function of surface type and depth under sea ice, towards improving primary production estimates.

Keywords: Under-ice downwelling average cosine; Under-ice spectral light field; Under-ice PAR propagation; Sea ice melt progression; Spring phytoplankton bloom; Arctic primary production

1 Introduction

Optical studies of the past decade have demonstrated that the inhomogeneous sea ice cover at different stages of melt causes a large spatial variability in the transmission of solar radiation to the underlying Arctic Ocean (e.g., Light et al., 2008; Ehn et al., 2011; Nicolaus et al., 2012; Katlein et al., 2015). The majority of transmitted light remaining under the sea ice is within the 400–700 nm spectral band termed photosynthetically active radiation (PAR) with shorter and longer wavelengths strongly attenuated within the overlying snow and ice cover. Snow depth primarily controls the amount of PAR transmitted to the water column (Nicolaus and Katlein, 2013). In the late spring, lower surface albedos of melting snow, developing melt ponds and white ice areas increase total under-ice PAR levels and drive pri-

mary production beneath the ice cover (Arrigo et al., 2014; Mundy et al., 2014). Simultaneously, enhanced differences in transmittance due to variation in surface type create a more complex radiation field beneath the ice cover, which is displayed in the diffuse vertical attenuation coefficient, K_d , and average cosine coefficient, μ_d , of downwelling irradiance in the water column. Frey et al. (2011) observed subsurface transmission peaks under white ice at 5–10 m water depth due to an order of magnitude larger light transmission through adjacent melt pond-covered ice. The lateral spreading of radiation also impacts the vertical diffuse attenuation coefficient, K , due to changes to the angular distribution of the under-ice radiation field (Ehn et al., 2011; Katlein et al., 2016; Massicotte et al., 2018). Experiments to determine underwater irradiance distributions have been undertaken by Voss (1989), Berwald et al. (1995) and Leppäranta et al. (2003); however, they have not been examined in detail for ice-covered conditions, where the ice cover plays an important role in the measurements of light availability for primary production esti-

* Centre for Earth Observation Science, University of Manitoba, Winnipeg, Manitoba, CA

† Takuvik, Université Laval and CNRS, Quebec City, Quebec, CA

Corresponding author: L. C. Matthes (matthesl@myumanitoba.ca)

mates, as algal cells indiscriminately absorb light from any direction. Bio-optical models of primary production in the open ocean showed an underestimation of phytoplankton growth by 5–13%, if the shape of the underwater light field is ignored and only downwelling planar irradiance is measured (Sathyendranath et al., 1989). Furthermore, a recent ice-ocean radiative transfer modelling study highlighted that scalar irradiance could be up to 1.85 times greater than downwelling planar irradiance immediately beneath the ice cover (Pavlov et al., 2017).

The average cosine for downwelling irradiance, μ_d , provides a tool to describe the angular distribution of the underwater radiation field (0.5 being isotropic, and 1.0 fully downward directed) and to relate spatial variability of the radiation field to the propagation of radiation in the atmosphere-ice-ocean system. This propagation generally follows an exponential decline with increasing depth from the water surface and can be modelled as a function of scattering and absorption processes (Kirk, 1981; Bannister, 1992; Mobley, 1994; Berwald, 1999). However, the high scattering of radiation while propagating through the sea ice causes the angular distribution of light penetrating the water column to be different from the open water scenario, which is largely controlled by the solar zenith angle (Kirk, 2011). Several studies have assumed that μ_d values beneath the ice cover are similar to those in open water at greater depths (Arrigo et al., 1991; Ehn and Mundy, 2013; Katlein et al., 2014), while others have assumed an isotropic light field (e.g., Frey et al., 2011). The lateral spreading of radiation caused by large-scale sea ice features, such as melt ponds, cracks and leads, is also expected to have an impact on μ_d , underlining the need for an improved understanding of the angular shape of vertical radiative transfer.

Direct observations of the average cosine may also help to classify the impact of the heterogeneous under-ice light field on irradiance readings obtained by different radiometer types. Measurements of photosynthetically active radiation (PAR) for primary production estimates are commonly performed with either scalar or cosine-corrected planar radiometers, although an underestimation of the prevailing light availability is known to occur with the latter (Morel and Gentili, 2004). Although scalar radiometer with a spherical collector that capture PAR from all directions provide a more realistic measurement for primary production, planar irradiance sensors are commonly used. Planar irradiance can be converted into scalar irradiance using the average cosine; however, more knowledge regarding changes to μ_d beneath a sea ice cover is needed. To study alterations of μ_d in the ice-covered water column, simultaneous measurements with both sensor types must be performed at several depth levels.

With increasing primary production over the period of ice melt, differences in light attenuation also alter the spectral composition of the radiant flux within the under-ice water column (Pavlov et al., 2017). Algal cells, detritus, dissolved organic matter and water itself absorb irradiance at specific wavelengths, which makes spectral irradiance measurements necessary to calculate PAR accurately. Differences in the spectral absorption also have an effect

on the conversion of irradiance units (Morel and Smith, 1974). For primary production estimates, PAR data are given in quantum units [$\mu\text{mol m}^{-2} \text{s}^{-1}$] instead of energy units [W m^{-2}] because photosynthesis is a photochemical process that depends on the number of photons absorbed rather than their energy content. Sensors for measuring the broad-band PAR quantum flux that can accommodate changes in the spectral shape of the underwater light field are available. However, ice mass balance buoys to measure the bio-optical properties of the surface water layer are equipped with shortwave radiation sensors. These frequently used sensors operate in energy units and need to be converted to quantum units for primary production studies.

Recognizing the need for an improved characterization of the under-ice light field, a dataset of spectral irradiance profiles beneath landfast sea ice was collected during the Green Edge ice-camp campaigns in May–June 2015 and June–July 2016. The objectives of this study were to: (1) describe the impact of the sea ice cover on coefficients to describe the spectral distribution of downwelling irradiance in the water column, particularly the downwelling average cosine, with increasing depth and over the course of spring melt; (2) quantify how changes in these coefficients affect under-ice PAR readings taken with a cosine planar versus a spherical scalar radiometer and stated in energy units versus quanta units; and (3) investigate the impact of different irradiance detector types on primary production estimates. Variations in the diffuse attenuation and average cosine of downwelling PAR are presented over the course of spring melt and related to a potential error that different measurements could have on primary production estimates.

2 Methods

2.1 Study area

Spectral irradiance measurements were conducted as part of the Green Edge project in 2015 and 2016 on landfast sea ice (67° 28.784' N, 63° 47.372' W) near Qikiqtarjuaq, Nunavut, Baffin Bay (**Figure 1a**). From 5 May to 8 June 2015, surface irradiance and under-ice spectral irradiance were measured prior to melt onset, under different snow depths and mostly overcast sky. The solar zenith angle ranged from 54° to 80° with a mean angle of 61°. In 2016, measurements began after snow melt onset, and spectral irradiance data were collected beneath sea ice covered with wet snow, shallow melt ponds and white ice between 14 June and 4 July. Sky conditions were characterized as cloudy with sunny intervals to fully overcast, long periods of fog and a solar zenith angle ranging from 45° to 73° with a mean angle of 59°. All measurements were performed around the ice camp in areas with undisturbed surfaces. Snow depth, h_s , melt pond depth, h_{MP} , the height of drained white ice above melt pond surface, h_{BP} , freeboard height of white ice above sea surface, h_{FB} , and ice thickness, h_i , were measured with a ruler at the sea ice surface above the under-ice irradiance measurement after each deployment of optical equipment. Melt pond coverage was estimated from unmanned aerial vehicle (UAV) photographs taken 90 m above the sampling area (**Figure 1b, c**).

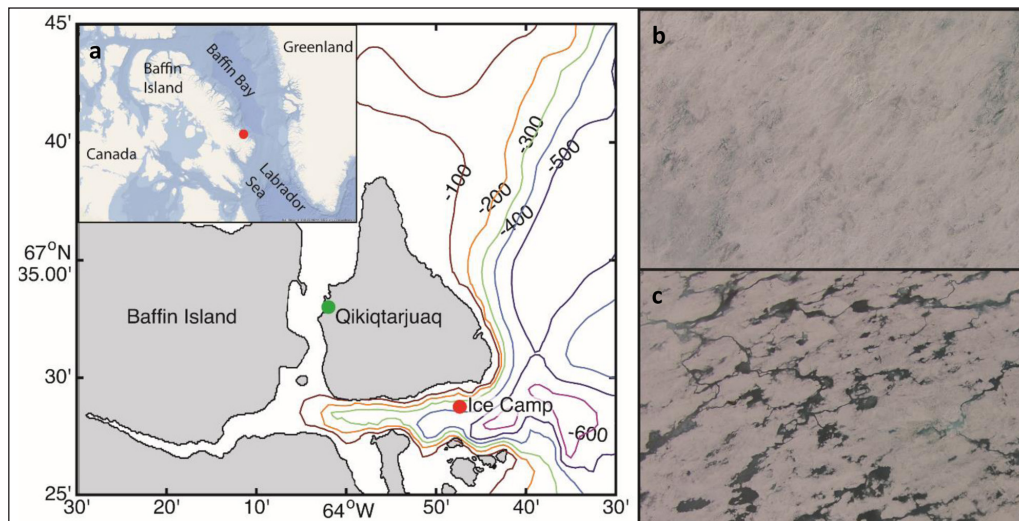


Figure 1: Study area. (a) Location of ice camp as part of the Green Edge campaign in 2015 and 2016 on landfast sea ice near Qikiqtarjuaq, Southern Baffin Island, NU, Canada (Courtesy of E. Rehm) and UAV photographs showing sea ice surface conditions in the sampling area on (b) 16 June and (c) 2 July 2016. DOI: <https://doi.org/10.1525/elementa.363.f1>

2.2 Irradiance measurements

At each sampling station, the optical set-up consisted of a surface reference radiometer which measured incident downwelling planar irradiance, $E_d(0, \lambda)$, and an under-ice arm equipped with three radiometers to measure transmitted downwelling planar irradiance, $E_d(z, \lambda)$, downwelling scalar irradiance, $E_{od}(z, \lambda)$, and upwelling scalar irradiance, $E_{ou}(z, \lambda)$, (Figure 2). These four hyperspectral radiometers (two planar RAMSES-ACC and two scalar RAMSES-ASC, TriOS GmbH, Germany) were equipped with internal pressure and tilt sensors and measure irradiance spectra in the wavelength range of 320 to 950 nm at a resolution of 3.3 nm (190 channels).

Spectral albedo, $\alpha(\lambda)$, of different sea ice surface features was measured prior to the under-ice light sampling. To achieve this, a planar radiometer was mounted on an aluminum pole 1.5 m away from the tripod and was turned upward to measure downwelling planar irradiance before it was turned downward to measure reflected planar irradiance. Spectral albedo was calculated as the average ratio of five consecutive downwelling and upwelling irradiance readings.

Transmitted irradiance beneath the sea ice cover was recorded using a custom-built double-hinged aluminum pole (hereafter L-arm) connected to a manual winch to lower the instrument array to greater water depths by attaching additional 1.5-m aluminum poles to the arm. The L-arm was deployed through a 20-inch auger hole, and the radiometers were positioned directly beneath the ice bottom 1.5 m south of the hole. Snow or shaved ice was placed back into the hole to minimize the influence of elevated light levels on under-ice measurements. For the investigation of spectral and PAR transmittance, the two planar radiometers, used as surface reference and under-ice sensor, were cross-calibrated in-air by simultaneously recording incident downward irradiance. Cross-calibration was performed following the equation provided in Antoine et al. (2013). Further steps of pre-analysis included the

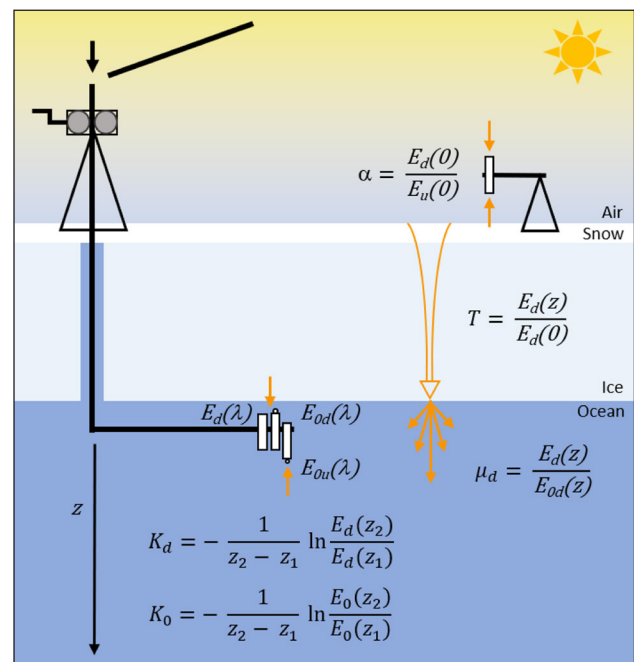


Figure 2: Schematic of optical equipment deployment and derived coefficients. Above the air-snow interface: measurement of spectral incident irradiance ($E_d(0)$) and spectral surface albedo (α); beneath the ice bottom via L-arm: measurement of transmitted downwelling planar and scalar irradiance spectra ($E_d(z)$, $E_{od}(z)$) and upwelling scalar irradiance ($E_{ou}(z)$). Spectral irradiance data were used to calculate transmittance (T), downwelling average cosine (μ_d) and diffuse vertical attenuation coefficient of downwelling (K_d) and scalar irradiance (K_0). DOI: <https://doi.org/10.1525/elementa.363.f2>

immersion correction of all under-ice light data due to the larger refractive index of water compared to air, and an exclusion from further analysis of data recorded when the vertical angle of the L-arm exceeded 5° from nadir.

In 2015, 17 vertical profiles of $E_d(0, \lambda)$, $E_{od}(z, \lambda)$, and $E_{ou}(z, \lambda)$ were collected in 0.4–0.5-m steps from approximately 0.1 m below the ice bottom to a water depth of 18 m. Due to no significant changes (Student's-T-test) of snow depth and sea ice thickness over the sampling period and much larger vertical angles, only five profiles with a snow depth exceeding 15 cm (thick snow cover) were used in the calculation of changes in transmittance, diffuse attenuation and the downwelling average cosine in the water column. Using the same protocol as that in 2015, in 2016 eleven under-ice irradiance profiles to a water depth of 20 m were recorded under different sea ice surface properties, including four measurements underneath thin snow-covered ice, three measurements below white ice and four measurements below ponded ice.

2.3 Chlorophyll *a* measurements

For the analysis of chlorophyll *a* (chl *a*) concentration in the sea ice bottom, the bottommost 3 cm of at least two ice cores were extracted at a thick snow site in 2015 and thin snow and white ice sites in 2016 in proximity to the optical measurements. No ice cores were collected in melt ponds. The detailed sampling method is described in Galindo et al. (2017). Water samples were taken at 1.5, 5, 10 and 20 m using Niskin bottles, while ice-water interface samples were collected at 0.5 m with a submersible pump (Cyclone®) mounted to an under-ice arm. In the laboratory, melted sea ice and water samples were filtered onto 25 mm GF/F filters using a vacuum pump, wrapped in aluminum foil and stored at -80°C until analysis. Total chl *a* concentration was determined by High Performance Liquid Chromatography (HPLC) following Ras et al. 2008.

2.4 Data analysis

In the following calculation of the coefficients, measured irradiance spectra were interpolated to 1-nm steps and vertical profiles of under-ice $E_d(z, \lambda)$, $E_{od}(z, \lambda)$ and $E_{ou}(z, \lambda)$ were calculated at 0.5-m steps from 1.5-m to 18-m (2015) or 20-m (2016) water depth using linear interpolation. Spectral irradiance and PAR transmittance through the ice cover at different stages of melt were estimated by dividing E_d measured at the ice bottom by E_d measured simultaneously at the ice surface. For the description of the angular structure of the under-ice light field, $\mu_d(z, \lambda)$ was calculated as the ratio of E_d to E_{od} for each profile. To provide average μ_d for the four surface types (thick snow, thin snow, white ice, ponded ice), a two-term power series model was fitted through the under-ice $\mu_d(\text{PAR})$ profiles of each surface type. Scalar under-ice irradiance $E_o(z, \lambda)$ was estimated by summing the coincident measurements of

E_{od} and E_{ou} . The vertical diffuse attenuation coefficient for downwelling irradiance $K_d(z, \lambda)$ was estimated by fitting an exponential curve ($R^2 > 0.96$) through the under-ice E_d profiles. To study differences between under-ice K_d and K_o , an exponential curve ($R^2 > 0.96$) was also fitted through the under-ice profile of E_o to estimate $K_o(z, \lambda)$. All calculations were also performed with the coefficients for PAR, which was integrated over the waveband 400–700 nm.

The investigation of a factor to convert under-ice PAR data, given in energy units into values stated in photon density, was undertaken by a spectral conversion of downwelling scalar irradiance measured in $\text{W m}^{-2} \text{nm}^{-1}$, $E_{od}(z)$, into the corresponding quantum irradiance given in $\mu\text{mol m}^{-2} \text{s}^{-1}$, $E_{od-Q}(z)$, as follows

$$E_{od-W}(z) = \int_{400}^{700} E_{od}(z) d\lambda \quad (1)$$

$$E_{od-Q}(z) = \int_{400}^{700} \frac{E_{od-W}(z) \lambda}{c h N_A} d\lambda \quad (2)$$

including the speed of light (c), Planck's constant (h) and Avogadro's number (N_A). Afterwards, the ratio $E_{od-Q}(z, \text{PAR})$ to $E_{od-W}(z, \text{PAR})$ was calculated for different stages of sea ice melt.

2.5 Statistical analysis

A normal distribution of the data set and the homogeneity of variances were confirmed, and a square root transformation was applied, if necessary, before parametric tests were used. To investigate differences in snow depth and ice thickness between the sampling years, a Student's T-test was performed. A one-way ANOVA was used to test for significant differences in PAR transmittance between surface types, followed by Tukey's HSD to identify significantly different groups. Additionally, differences between planar and scalar irradiance measurements, as well as differences in the downwelling average cosine, $\mu_d(\text{PAR})$, and in the E_Q/E_W ratio with changing surface types and increasing depth were tested using a two-way ANOVA.

3 Results and Discussion

3.1 Sea ice surface

The conditions on the sea ice surface displayed a strong contrast between sampling years (Table 1). Snow depths in 2015 varied between 7 and 32 cm with snowfall events in the end of May and were significantly higher than in 2016 ($t = 2.5211$, $df = 18$, $p < 0.05$). Measured surface albedo was very high, averaging 0.95 in the PAR range. Ice thickness did not decrease, and no surface flooding

Table 1: Average \pm standard deviation snow depth (\bar{h}_s), height of white ice above melt pond surface (\bar{h}_{wt}), melt pond depth (\bar{h}_{MP}), ice thickness (\bar{h}_i), and freeboard (\bar{h}_{FB}) by sampling year. DOI: <https://doi.org/10.1525/elementa.363.t1>

Year	\bar{h}_s (cm)	\bar{h}_{wt} (cm)	\bar{h}_{MP} (cm)	\bar{h}_i (m)	\bar{h}_{FB} (cm)
2015	23 ± 8^a	— ^b	—	1.24 ± 0.06	4 ± 4
2016	11 ± 6^a	5 ± 2	5 ± 3	1.19 ± 0.12	9 ± 3

^a Shared superscripts represent statistically significant differences: $p < 0.05$.

^b Dash indicates no melt ponds or white ice had formed during the sampling period.

was observed in the sampling area during the period of the irradiance measurements in this study. Additional description of the environmental conditions are available elsewhere (Oziel et al., 2019).

In mid-June 2016, air temperatures were above the freezing point, and the ice surface was covered with a relatively wet snow cover displaying a mean albedo of 0.73 in the PAR spectral range which corresponds to reported albedo values of melting snow (Figure 1b; Perovich, 1996). Shortly after, snow melt and a rain event on 22 June acted to rapidly flood the ice surface. Snowfall and freezing surface water due to low air temperatures during the night slowed down surface melt during the following days. By 27 June, large, but shallow melt ponds were visible at the ice surface (Figure 1c). Surface PAR albedos of melt ponds and bare ice averaged 0.33 and 0.57, respectively, and lay in the reported range for ponded and white ice (Perovich, 1996). Melt pond coverage of the ice surface reached 17–27% within the sampling area; however, melt ponds became smaller at the end of June due to increased surface drainage (Oziel et al., 2019). Ice thickness also began to decrease from >1.2 m at the end of June to <1.0 m by 4 July, but was not significantly different from that of 2015 ($t = 1.4931$, $df = 26$, $p = 0.147$).

3.2 Spectral and PAR transmittance

The change from a thick snow cover in May 2015 to wet snow in mid-June 2016 to ponded and white ice by the end of June resulted in a significant increase in the transmittance of light through landfast sea ice of the same thickness ($F_{3,12} = 39.64$, $p < 0.001$; Table 2). Transmittance profiles for selected spectral bands and PAR in the water column beneath different ice surface types are shown for selected days in the supplemental material (Figure S1). In 2015, new snowfall events caused low transmission of surface radiation through the highly reflective snow-covered sea ice, which then decreased monotonically with water depth. Spectral transmittance peaked between 470 and 570 nm reflecting the high absorption of snow and ice in the longer wavelength spectrum. In 2016, transmission through ice with a thin layer of wet snow was significantly larger with a more pronounced peak of spectral transmittance at wavelengths between 470 and 500 nm beneath the ice bottom. Light transmission through white ice was of the same magnitude. However, vertical spectral transmittance profiles showed a small increase in the 400 to

600 nm wavelength spectrum in the first 3 m below the ice bottom due to higher light transmission through adjacent melt ponds. The typical exponential decline of transmittance was observed beneath ponded ice.

Observations undertaken in 2016 during melt pond formation showed that the initial increase in under-ice light levels was caused by snow melt onset, which likely caused the surface albedo to be much lower in mid-June 2016 in comparison to very high albedos observed in late-May 2015. PAR transmittance of white and ponded ice corresponded with that presented in the literature (Ehn et al., 2011; Light et al., 2015). PAR transmittance recorded during snow melt was of the same magnitude as the transmission of PAR through the subsequent white ice, although the surface albedo of wet snow was greater. The similarity implies an increased light attenuation within the white ice layer. Ice algae, which were observed in the ice bottom in both years, could have influenced the transmitted light spectra. However, measured ice algae chl *a* concentration decreased from 3.476 mg m^{-2} to 0.267 mg m^{-2} over the sampling period. Instead, scattering within the drained surface layer of white ice, which consisted of large melt-grain clusters permeated by void space, could have caused a stronger light attenuation than the likely water-saturated snow layer at the snow-ice-interface (Light et al., 2008).

3.3 Vertical diffuse attenuation in the water column

During the 2015 pre-melt study, the thick snow and ice layer was associated with a very diffuse radiation field in the water column and a small $K_d(\text{PAR})$ between 0.08 and 0.14 m^{-1} (Figure 3a). Over the sampling period, $K_d(\text{PAR})$ decreased to a relatively constant value at the end of May, while the difference between K_o and K_d increased from 4 to 18%. In the following year, $K_d(\text{PAR})$ increased by a factor of two from 0.09 m^{-1} to 0.23 m^{-1} (Figure 3b). The difference between the two coefficients decreased from 8 to 3%.

The variations in $K_d(\text{PAR})$, and $K_o(\text{PAR})$ with depth and ongoing melt progression may have been related to a change in the absorption of PAR by algae cells in the water column. In 2015, average chl *a* concentration in the first 20 m of the surface water layer varied between $0.177 \text{ } \mu\text{g L}^{-1}$ and $0.135 \text{ } \mu\text{g L}^{-1}$ until it dropped to $0.035 \text{ } \mu\text{g L}^{-1}$ on 29 May. Afterwards chl *a* increased again to a value of $0.159 \text{ } \mu\text{g L}^{-1}$ on 6 June. PAR attenuation in the

Table 2: Post-hoc comparison of average PAR transmittance (T) \pm standard deviation through landfast sea ice with different surface types in 2015 (thick snow) and 2016 (thin snow, white ice, melt pond). DOI: <https://doi.org/10.1525/elementa.363.t2>

Group	<i>n</i>	$T(\text{PAR})$	Tukey's HSD comparisons		
			Thick snow	Thin snow	White ice
Thick snow	5	0.003 ± 0.0008	— ^a	—	—
Thin snow	4	0.118 ± 0.05	$p < 0.001$	—	—
White ice	3	0.121 ± 0.04	$p < 0.001$	—	—
Melt pond	4	0.264 ± 0.05	$p < 0.001$	$p < 0.05$	$p < 0.05$

^a Dash indicates no significant differences observed.

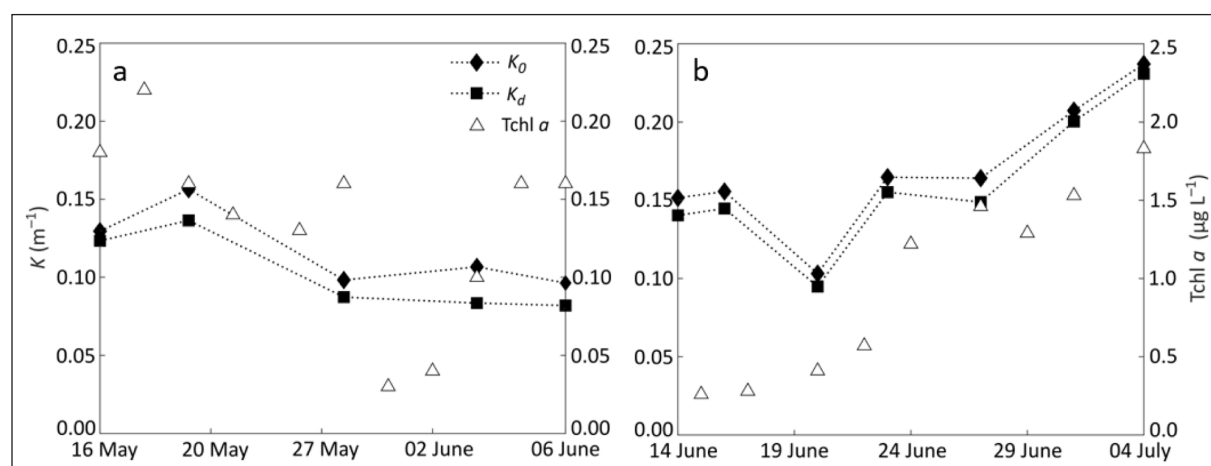


Figure 3: Vertical diffuse attenuation of downwelling planar PAR (K_d) and scalar PAR (K_0). Coefficients were measured beneath landfast sea ice in (a) 2015 and (b) 2016. Total chlorophyll *a* (Tchl *a*) is given as average concentration in the first 20-m depth. DOI: <https://doi.org/10.1525/elementa.363.f3>

water column only decreased slightly with the decline in chl *a* concentration. In 2016, vertical diffuse attenuation increased with ongoing melt progression due to enhanced absorption and scattering caused by an increase in average chl *a* concentration from $0.258 \mu\text{g L}^{-1}$ on 15 June to $1.828 \mu\text{g L}^{-1}$ on 4 July in the upper 20-m water column. Furthermore, phytoplankton cells are mainly forward-scattering which could have influenced a decrease of the difference between K_d and K_0 .

To study differences in diffuse attenuation of transmitted irradiance with increasing depth, K_d and K_0 were calculated between 3 and 6 m and between 6.5 and 18 m for the 2015 dataset (Table S1), as well as between 1.5 and 6 m and between 6.5 and 20 m for the 2016 dataset (Table S2), based on an observed smaller decrease in transmittance in the water column below 6-m depth (data not shown). The difference between K_0 and K_d was 22%, whereas in 2016, the melting ice cover displayed a 9% greater K_0 in the first 6-m water depth. In both years, the radiant flux became more downward-directed and less impacted by differences in light transmission through the sea ice cover with greater water depths resulting in only an 11% greater K_0 than K_d between 6.5- and 18-m depths in 2015 and 4% greater K_0 between 6.5 and 20 m in 2016.

Diffuse attenuation coefficients largely varied directly beneath the ice bottom with the change in ice surface from a wet snow cover to a mixture of bare ice and melt ponds. Light exiting the snow-covered ice layer in 2015 was more diffuse due to the highly scattering dry snow conditions (see next section), leading to a greater difference between K_d and K_0 . Leppäranta et al. (2003) reported a 10% larger K_0 in snow- and ice-covered lakes, as well as a decrease in the difference between the two coefficients after the artificial removal of the scattering snow cover. Our results show the same trend with ongoing surface melt, whereby the large portion of longer wavelengths, which penetrate through the ponded ice cover and are absorbed strongly in the surface water layer, may have also contributed to a decrease between K_d and K_0 .

3.4 Differences between under-ice planar and scalar irradiance profiles

Comparing irradiance profiles recorded with planar versus scalar radiometers, surface type ($F_{3,24} = 14.25$, $p < 0.001$) and depth ($F_{1,24} = 43.97$, $p < 0.001$) had a significant effect on the discrepancy between the recorded downwelling planar and scalar irradiance profiles in both years. Summarizing the 2015 dataset, measurements of $E_{\text{od}}(\text{PAR})$ at 3-m and at 18-m water depths were on average 38 and 32% larger, respectively, than simultaneous $E_d(\text{PAR})$ readings. Upwelling scalar irradiance, $E_{\text{ou}}(\text{PAR})$, was an order of magnitude less, resulting in a slightly higher $E_o(\text{PAR})$ of 3% compared to $E_{\text{od}}(\text{PAR})$ throughout the entire water column. In 2016, the difference between $E_{\text{od}}(\text{PAR})$ and $E_d(\text{PAR})$ was lower, between 31 and 34% at 3 m and between 25 and 28% at 20-m depth, due to overall greater light transmission through the sea ice cover. $E_{\text{ou}}(\text{PAR})$ was again within 3% of that of $E_{\text{od}}(\text{PAR})$.

The under-ice irradiance levels were low under the snow-covered sea ice in 2015 with downwelling scalar PAR never exceeding $4.9 \mu\text{mol m}^{-2} \text{s}^{-1}$ (Figure S2a). Under-ice PAR levels were 30 times higher after the beginning of surface melt in June 2016, reaching mean $E_{\text{od}}(\text{PAR})$ values of $151.8 \mu\text{mol m}^{-2} \text{s}^{-1}$ during snow melt, and 105.5 and $280.3 \mu\text{mol m}^{-2} \text{s}^{-1}$ beneath white and ponded ice at 1.5-m depth, respectively (Figure S2b–d). Fog events became more frequent by the end of June which caused lower incident radiation levels. Irradiance profiles recorded below white and ponded ice shortly after each other also illustrated a decreasing impact of the heterogeneous light transmission on the under-ice PAR levels with increasing depth (Figure 4). The decrease in PAR with depth was greater under melt ponds than that under white ice until 10 m where the curves became parallel and, therefore, PAR propagation was no longer influenced by the sea ice cover.

3.5 Under-ice downwelling average cosine

The measured irradiance spectra, $E_d(\lambda)$ and $E_{\text{od}}(\lambda)$, and the calculated spectral downwelling average cosine, $\mu_d(\lambda)$, are shown for specified depths in Figure 5. Changes in the

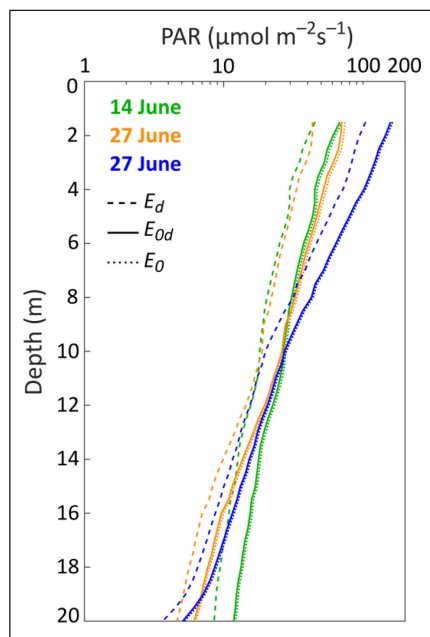


Figure 4: Interpolated profiles of measured under-ice PAR. Plotted as downwelling planar irradiance E_d (dashed lines), downwelling scalar irradiance E_{od} (solid lines) and scalar irradiance E_o (dotted lines) beneath snow-covered sea ice on 14 June (green), white ice on 27 June (orange), and ponded ice on 27 June (blue) 2016. DOI: <https://doi.org/10.1525/elementa.363.f4>

spectral shape of downwelling radiation with increasing depth had an impact on $\mu_d(\lambda)$. On 16 May 2015, light levels were exceedingly low and diffuse due to the thick snow cover which resulted in relatively constant $\mu_d(\lambda)$ values between 400 and 600 nm with a low at 490 nm (**Figure 5a**). Above 600 nm, irradiance was rapidly attenuated in the water column. In 2016, the spectral shape of $\mu_d(\lambda)$ demonstrated a wavelength dependence. Beneath snow-covered sea ice at 1.5-m depth, the lowest $\mu_d(\lambda)$ of 0.65 was measured at 431 nm and slightly increased to 0.66 at 400 nm on 14 June. A much stronger increase in $\mu_d(\lambda)$ was measured towards longer wavelengths (indicating a more downwards directed irradiance field) with ratios of 0.72 at 700 nm. Enhanced noise for $\mu_d(\lambda)$ was observed below 10-m depth due to the reduction in irradiance levels. With ongoing surface melt, the smallest $\mu_d(\lambda)$ values of 0.69 shifted from the blue towards the green part of the spectrum at 487 nm at 1.5 m on 4 July (**Figure 5b–d**). The low transmission and strong attenuation of spectral irradiance >600 nm caused uncertainty in the calculation of the average cosine above 600 nm due to the detection limit of the sensor. However, irradiance values of the red spectrum were so low that they were not expected to have an impact on the calculation of $\mu_d(PAR)$.

The angular distribution of downwelling radiation in the photosynthetic waveband below landfast ice cover varied significantly with surface type ($F_{3,24} = 15.54$,

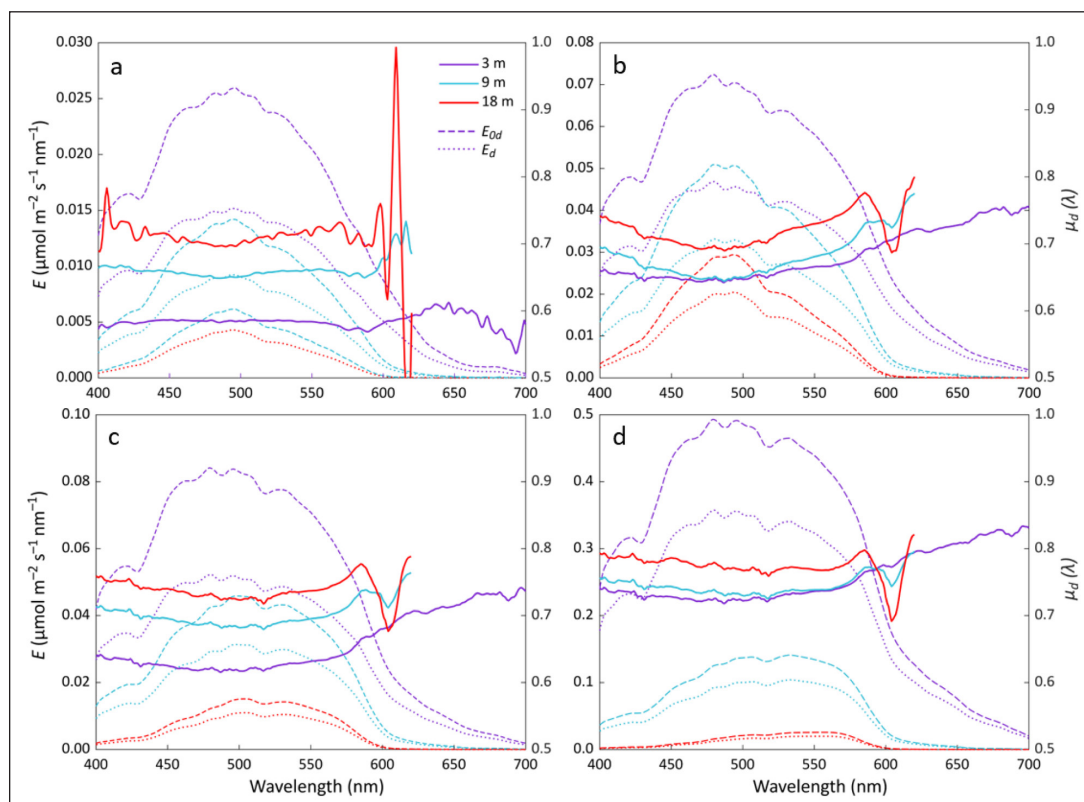


Figure 5: Spectral downwelling under-ice irradiance and downwelling average cosine of spectral irradiance. Measurements of spectral E_d (dotted lines) and E_{od} (dashed lines) were performed **(a)** beneath snow-covered ice on 16 May 2015, **(b)** beneath snow-covered ice on 14 June 2016, **(c)** beneath white ice on 27 June 2016, and **(d)** beneath ponded ice on 4 July 2016. Spectral irradiance and spectral μ_d (solid lines) are plotted for three depths. DOI: <https://doi.org/10.1525/elementa.363.f5>

$p < 0.001$) as well as with the change in the shape of the spectra with depth ($F_{1,24} = 62.38$, $p < 0.001$; **Figure 6**). In 2015, the PAR light field was nearly isotropic displaying significantly lower downwelling average cosines, $\mu_d(\text{PAR})$, at 3-m depth below ice that was covered with a >15-cm thick snow layer than in 2016 (**Table 3**). The snow layer as a highly scattering medium caused the most diffuse light field directly beneath the ice bottom. With increasing depth, $\mu_d(\text{PAR})$ significantly increased, similarly to those

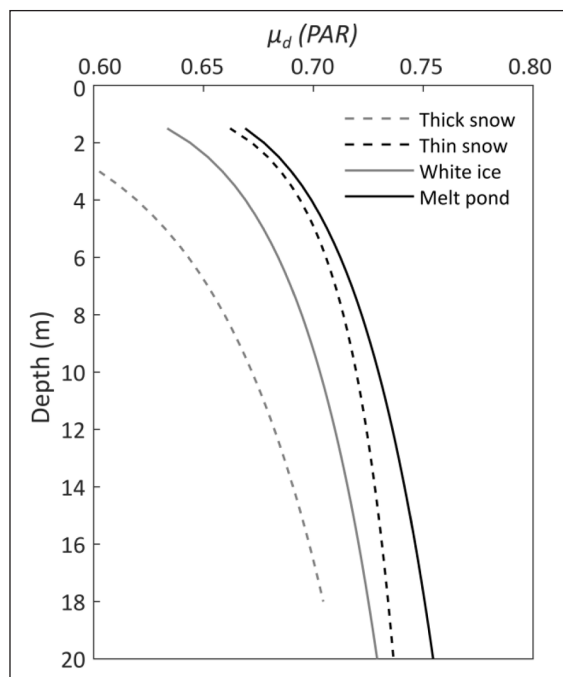


Figure 6: Downwelling average cosine ($\mu_d(\text{PAR})$) beneath different sea ice surface types. Mean $\mu_d(\text{PAR})$ was calculated from vertical irradiance profiles beneath sea ice with a thick snow cover in 2015 and beneath ice with a thin snow cover, ponded and white ice in 2016. DOI: <https://doi.org/10.1525/elementa.363.f6>

observed in the following year at the same depth level. In 2016, the PAR light field was more downward-directed associated with a greater light transmission through the sea ice cover. At the ice bottom, μ_d values for PAR did not vary significantly between ice surface properties, but continuously increased with depth; $\mu_d(\text{PAR})$ measured at 18 m beneath ponded ice was significantly greater than that at 3 m. Furthermore, $\mu_d(\text{PAR})$ in the water column beneath snow-covered ice showed substantially less change with depth below 10 m than those under white and ponded ice.

Light propagation became more downward-directed ($\mu_d > 0.7$) with the transition from a thick snow cover to a mosaic of white ice and melt ponds due to an increased light transmission. Downwelling average cosine values, stated in the literature, range from 0.56 to 0.7 directly beneath the sea ice bottom, which corresponds well with our field observations (Arrigo et al., 1991; Ehn and Mundy, 2013; Katlein et al., 2014). Diffuse incoming radiation caused by clouds and fog also play a role in the under-ice light propagation. The frequent fog events in late June 2016 could have had an effect on the lower μ_d beneath white ice compared to sea ice with a thin snow layer.

Variations in the propagation of downwelling irradiance with increasing depth were recently examined numerically for an ice-covered water column north of Svalbard as the ratio of E_o/E_d in the PAR spectrum. In the model, the sea ice was covered with a thin snow layer. Ratios of E_o/E_d are presented for pre-bloom and bloom conditions based on the output from a radiative transfer model (Pavlov et al., 2017). A reversal of this ratio allows for a reasonable comparison against our μ_d results, as E_o is not expected to be much larger than E_{od} in the water column. Modelled values stated by Pavlov et al. (2017) were a near constant 0.55 at the ice bottom (indicating that the model produces a nearly isotropic light field at the base of the ice cover independent of irradiance level), and then increased with depth to 0.7 during pre-bloom conditions and to 0.65 during a phytoplankton bloom at 40-m depth. Based

Table 3: Post-hoc comparison of mean downwelling average cosine ($\mu_d(\text{PAR})$) \pm standard deviation beneath landfast sea ice with different surface types: thick snow (Tks) in 2015 and thin snow (Tns), white ice (WI), and melt pond (MP) in 2016. DOI: <https://doi.org/10.1525/elementa.363.t3>

Surface type	Depth (m)	$\mu_d(\text{PAR})$	Tukey's HSD comparisons			
			$\mu_{d-\text{Tks}}$ (PAR, 3 m)	$\mu_{d-\text{Tns}}$ (PAR, 3 m)	$\mu_{d-\text{WI}}$ (PAR, 3 m)	$\mu_{d-\text{MP}}$ (PAR, 3 m)
Thick snow	3	0.61 ± 0.01	— ^a	—	—	—
	18	0.70 ± 0.02	$p < 0.001$	—	—	—
Thin snow	3	0.69 ± 0.02	$p < 0.001$	—	—	—
	18	0.73 ± 0.01	$p < 0.001$	—	—	—
White ice	3	0.66 ± 0.02	$p < 0.05$	—	—	—
	18	0.72 ± 0.02	$p < 0.001$	—	—	—
Melt pond	3	0.69 ± 0.03	$p < 0.001$	—	—	—
	18	0.75 ± 0.01	$p < 0.001$	$p < 0.05$	$p < 0.001$	$p < 0.01$

^a Dash indicates no significant differences observed.

on measured under-ice irradiance, our results showed the same trend of a decreasing $\mu_d(\text{PAR})$ with depth. However, measured $\mu_d(\text{PAR})$ was higher and varied between 0.61 and 0.69 directly beneath the ice bottom.

In the ice-covered water column, scattering and absorption processes control the propagation of light. Both processes determine changes in the angular distribution of light, while absorption alone impacts the spectral shape and creates a downward-directed light field weighted toward blue-green wavelengths with increasing depth. Measurements in 2015 recorded very low under-ice irradiance levels and only small changes in $\mu_d(\text{PAR})$, which indicate a low impact of PAR-absorbing and -scattering particles in the water column. Hence, light attenuation was mainly influenced by the high absorption coefficient of water itself, which dominated the rate of change in the average cosine mainly in the red portion of the spectrum. Blue-green light is weakly absorbed by water and, therefore, shows a greater reflectance which overlaps with the observed low of $\mu_d(\lambda)$ at 490 nm (Morel and Gentili, 2004).

In 2016, measured under-ice irradiance profiles showed an enhanced attenuation of light between 400 and 500 nm toward the end of June, influenced by an increase in phytoplankton biomass in the surface water layer. The implications on the under-ice light field can be seen in an increased rate of change of $\mu_d(\text{PAR})$ below white and ponded ice compared to the mean $\mu_d(\text{PAR})$ profile measured in the beginning of June beneath ice with a thin snow layer (Table 3, Figure 5b–d). Furthermore, the increased concentration of phytoplankton and absorption of wavelengths at the chlorophyll maxima led photons of the green spectrum to penetrate deepest and caused the observed depression in spectral μ_d at 487 nm due to a greater reflectance in the water column (Morel and Gentili, 2004). Pavlov et al. (2017) also postulated an increase in E_o compared to E_d under bloom conditions due to enhanced backscattering of algal cells. Although eukaryotic cells are described as weak backward-scatterers due to their large cell size (Kirk, 2011), the unique colonial aspect of *Phaeocystis pouchetii*, the nanoflagellate observed in Pavlov et al. (2017), could potentially influence backscatter more. More research on the subject is required. Our results showed a decline in the differences between E_{od} and E_d with negligible E_{ou} over sea ice melt progression and increased chl *a* concentration which suggests a stronger impact of the overall larger light transmission to the ocean rather than the elevated scattering by particles on the under-ice light propagation in spring. Note, however, that average chl *a* concentration in the water column only reached $1.8 \mu\text{g L}^{-1}$ during our study in 2016, in comparison to $7.5 \mu\text{g L}^{-1}$ in Pavlov et al. (2017).

Discrepancies between E_d and E_{od} are dependent on the relative importance of scattering versus absorption. A very diffuse underwater light field due to a low sun angle and/or multiple scattering in the overlying snow and ice cover increases the discrepancy between planar and scalar measurements, which can cause a large error in the measurement of light availability for the estimation of polar primary production. Hence, the use of planar irradiance E_d instead of scalar irradiance E_o in primary production

studies will always represent an underestimate of the prevailing underwater light conditions that needs to be corrected (Morel and Gentili, 2004; Kirk, 2011; Pavlov et al., 2017). To show percentage difference in primary production estimates resulting from planar vs. scalar PAR input, depth-integrated daily production was calculated for light-limiting conditions in surface waters on 14 June and light-saturating conditions on 1 July 2016. Averaged hourly surface irradiance, recorded over a period of 24 hours, together with the presented coefficients of light transmission through snow-covered, ponded and white ice and with $K_d(\text{PAR})$, were used to calculate vertical under-ice profiles of planar and, by using an average cosine of 0.7, scalar irradiance. Hourly photosynthetic rate was calculated with parameters gained from photosynthesis vs. irradiance (PvsE) curves of phytoplankton communities sampled at the ice camp. A maximum photosynthetic rate, P_{max} of $0.83 (0.25) \text{ mg C chl } a^{-1} \text{ h}^{-1}$, light saturation point, E_k of $59 (102) \mu\text{mol m}^{-2} \text{ s}^{-1}$ and photoinhibition, β , of $7.9 \times 10^{-4} (9.4 \times 10^{-5})$ of communities sampled on 14 June (1 July) were applied in the equation stated in Platt et al. (1980) and normalized to the chl *a* concentration measured from 0.5-m to 60-m depth. Afterwards, primary production rates were integrated over a depth of 60 m and over 24 hours.

Results indicate that once photosynthesis is saturated, the impact of the average cosine on calculated primary production rates is minimal. Figure 7 shows a 3% higher daily carbon production calculated with E_{od} instead of E_d on 1 July. The importance of using the scalar irradiance for production estimates is more pronounced in the pre-bloom period when light availability is still limiting photosynthesis and under-ice phytoplankton communities are adapted to low-light conditions. Depth-integrated daily carbon production was 16% lower using E_d instead of E_{od} due to the linear relationship between the rate of photosynthesis and increasing light levels before

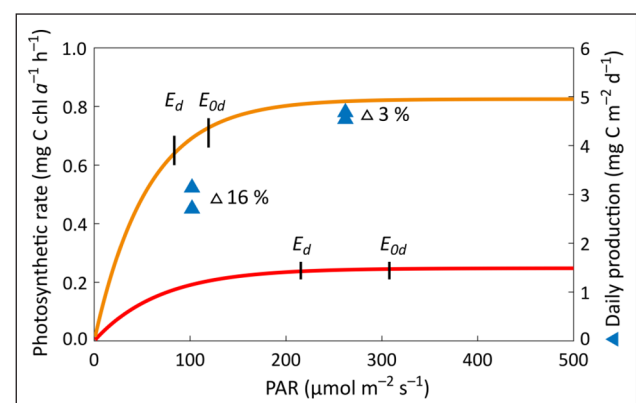


Figure 7: PvsE curves of phytoplankton and calculated daily carbon production in the ice-covered water column. Depth-integrated primary production at the sampling site down to 60 m was derived from PvsE curves of phytoplankton communities sampled on 14 June (orange, 16%) and on 1 July 2016 (red, 3%). Black lines show $E_d(\text{PAR})$ and $E_{od}(\text{PAR})$ values at 2-m depth at 12:00 pm. DOI: <https://doi.org/10.1525/elementa.363.f7>

reaching saturation levels. We note these estimates fall slightly below and above the range of 5–13% modelled by Sathyendranath et al. (1989). To avoid possible discrepancies in production estimates, scalar radiometers should be utilized, particularly in studies investigating the timing of under-ice blooms. If only downwelling planar irradiance is measured, an average cosine of 0.6 beneath snow-covered sea ice and 0.7 beneath ponded and white ice can be used to convert these under-ice measurements into downwelling scalar irradiance.

3.6 PAR unit conversion factors

Knowledge about the relation between total quanta and total energy at different depths also plays a relevant role in the conversion of underwater irradiance data. In biological studies, PAR data are commonly stated in units of $\mu\text{mol m}^{-2} \text{s}^{-1}$ (E_Q), while energy balance studies use units of W m^{-2} (E_W). Often the comparison between results from the two disciplinary fields is unclear because irradiance data are usually converted spectrally and conversion ratios for PAR data are lacking. The E_Q/E_W ratio for PAR is dependent on water transparency and depth and was studied for

several open water bodies (Morel and Smith, 1974; Reinart et al., 1998). This study investigated variations in the ratio spectrally and was used to study changes in the conversion factor of $E_{od}(PAR)$ values directly.

The highest and significantly different ratios were observed in profiles near the ice bottom ($F_{1,24} = 16.16$, $p < 0.001$) due to spectral narrowing as light propagates downward in the water column (Table 4). With increasing chl *a* concentration in the water column, profiles became C-shaped with a minimum between 6- and 10-m depth before again increasing at further depth. Figure 8a presents the calculated E_Q/E_W ratio of $E_{od}(PAR)$ with increasing depth in 2015. Below the ice bottom at 3-m depth, mean ratios of 4.24 were reached while a mean ratio of 4.14 was measured at 18-m depth. The observed differences in the ratios over time were related to variations in the spectral shape of transmitted irradiance (Figure 8b). The greatest ratio of 4.32, measured on 6 June at 3-m depth, was caused by a high transmission of longer wavelengths between 550 and 600 nm with a lower energy content. In contrast, on 16 May noticeably less irradiance between 550 and 600 nm, but more between 450 and 500 nm (photons

Table 4: Average ratio $E_Q/E_W \pm$ standard deviation beneath landfast sea ice with different surface types at two depth levels (3 m, 18 m). DOI: <https://doi.org/10.1525/elementa.363.t3>

Depth (m)	Ratio E_Q/E_W Surface type			
	Thick snow	Thin snow	White ice	Melt pond
3 m	4.24 ± 0.05	4.26 ± 0.03^a	4.24 ± 0.01	4.26 ± 0.02
18 m	4.15 ± 0.01	4.14 ± 0.01^a	4.20 ± 0.04	4.26 ± 0.07

^a Shared superscripts represent statistically significant differences: $p < 0.05$.

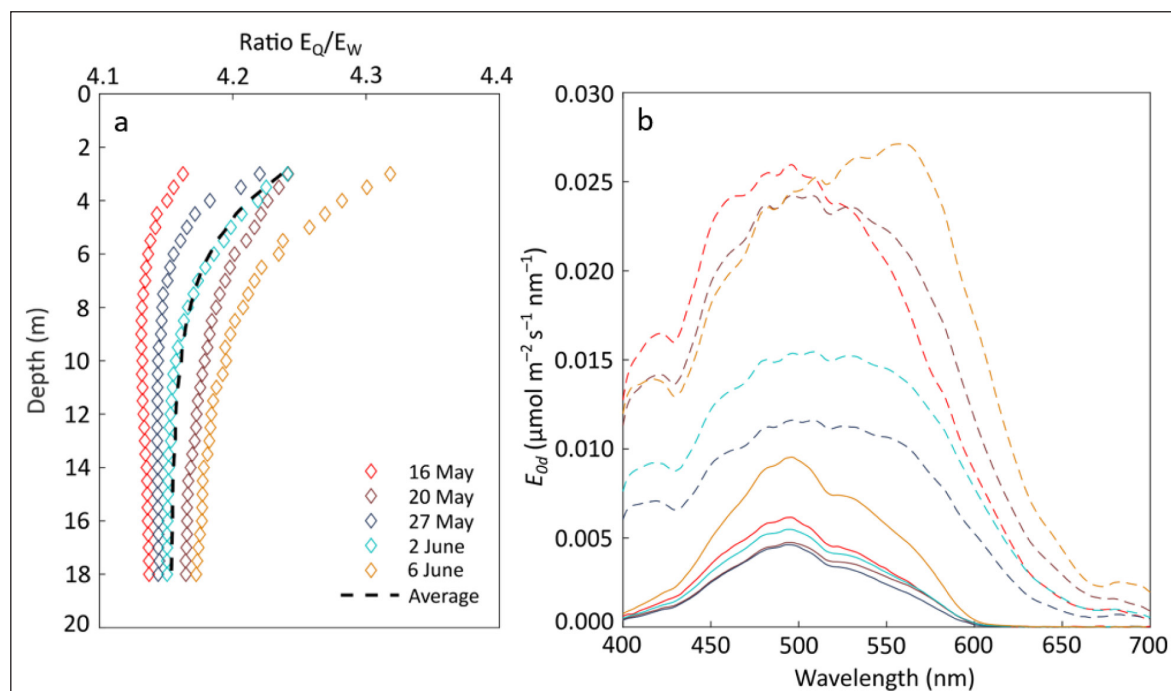


Figure 8: The ratio E_Q/E_W and spectral shape of scalar under-ice irradiance. (a) Vertical profile of ratio E_Q/E_W and (b) transmitted spectral scalar irradiance at depths of 3 m (dashed lines) and 18 m (solid lines) measured beneath snow-covered sea ice in 2015. Mean ratio stated as calculated average of 5 days. DOI: <https://doi.org/10.1525/elementa.363.f8>

with a higher energy content), were transmitted which resulted in a smaller ratio of 4.16 at the same depth level. The reason for a spectral shift in transmitted irradiance is likely a change in the ice algal biomass in the bottom-ice layer. Within the sampling period, the chl *a* concentration in the last 3 cm of the ice bottom varied from 3.8 mg m⁻² on 16 May to over 31.8 mg m⁻² on 27 May and 0.5 mg m⁻² on 2 June (Galindo et al., 2017), which contributed to the decrease in the transmission of wavelengths between 400 and 500 nm at the end of May and, thus, caused lower ratios. Water column chl *a* concentration was low (<0.2 µg L⁻¹) throughout the sampling period and had only a small impact on the spectral composition of PAR.

In 2016, measured E_Q/E_W ratios varied less beneath the ice bottom (Table 4) which could have been related to a low chl *a* concentration in the bottommost 3 cm of the ice layer never exceeding 3.5 mg m⁻² throughout the sampling period. However, only beneath sea ice with a thin snow cover, the ratio decreased significantly with depth likely due to a low light absorption by algal cells in the water column (Figure 9a). The chl *a* concentration was less than 0.3 µg L⁻¹. Beneath white and ponded ice (Figure 9b, c), the water column showed characteristics of blue-green waters (Morel and Smith, 1974). The increase in light attenuation by increased phytoplankton biomass altered the spectral composition of the radiant flux, so that photons of the green spectrum traveled deepest causing a greater ratio. The increase in the ratio with depth, observed beneath ponded ice, also emphasizes a chlorophyll maximum at greater depths. Generally, the E_Q/E_W ratio of 4.25 can be used to convert PAR given in watt units and measured directly beneath the ice. Morel and Smith (1974) provide an E_Q/E_W ratio of $4.15 \pm 10\%$ for a PAR unit conversion in the open water which encompasses with our observations. Another aspect that can be drawn from the spectral composition of downwelling irradiance is the observed change in the quality of PAR.

The efficiency of photosynthetic processes depends on how well the spectral composition of PAR matches the absorption spectrum of algal pigments, so that a shift of the radiant flux towards the green spectrum results in a lower quality of PAR and, thus, lower efficiency in the utilization of radiant energy by phytoplankton (Morel, 1978; Morel, 1991). As shown, the spectral shape of transmitted irradiance varied with increasing chl *a* concentration and has to be considered in the discussion of light availability for primary production.

Understanding the spring bloom dynamics of phytoplankton in the Arctic is of key importance to make predictions about the biological productivity in the Arctic marine environment in future. A significant fraction of the primary production takes place beneath a sea ice cover and commences during the spring–summer transition, when the sea ice cover starts to melt, and lasts until nutrients become limiting (Mundy et al., 2014; Barber et al., 2015). To understand and predict the timing and intensity of the spring bloom under Arctic sea ice, knowing how much PAR is available in the surface layer of the water column is important. Whereas energy balance studies require the flux of solar radiation energy incident onto the surface for calculating, e.g., radiative heating or melting rates, estimates of primary production require information of the total flux of photons in the PAR wavelength range from all directions at a given point in the water column or, in other words, the scalar irradiance, $E_{o,Q}(PAR)$.

The dependence of transmitted PAR propagation in the under-ice water column (e.g., transmission, vertical diffuse attenuation and downwelling average cosine) on the state of surface melt have been summarized in Figure 10 to assist with parametrization of the under-ice light field in polar primary production studies. The schematic figure presents the coefficients required to link PAR measured (1) above and below a melting landfast sea ice cover in spring, (2) in different units and (3) with different radiometer

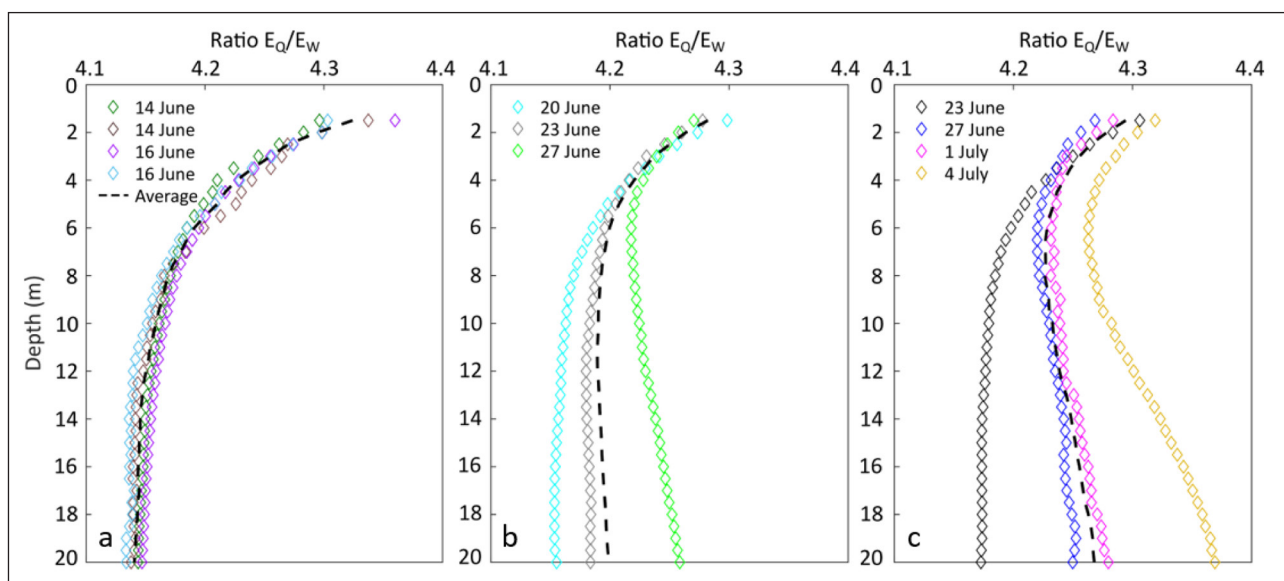


Figure 9: The ratio E_Q/E_W beneath sea ice with different surface types. Vertical profiles of the ratio measured (a) beneath snow-covered sea ice, (b) white ice and (c) ponded ice in 2016. Mean coefficient stated as calculated average for each surface type. DOI: <https://doi.org/10.1525/elementa.363.f9>

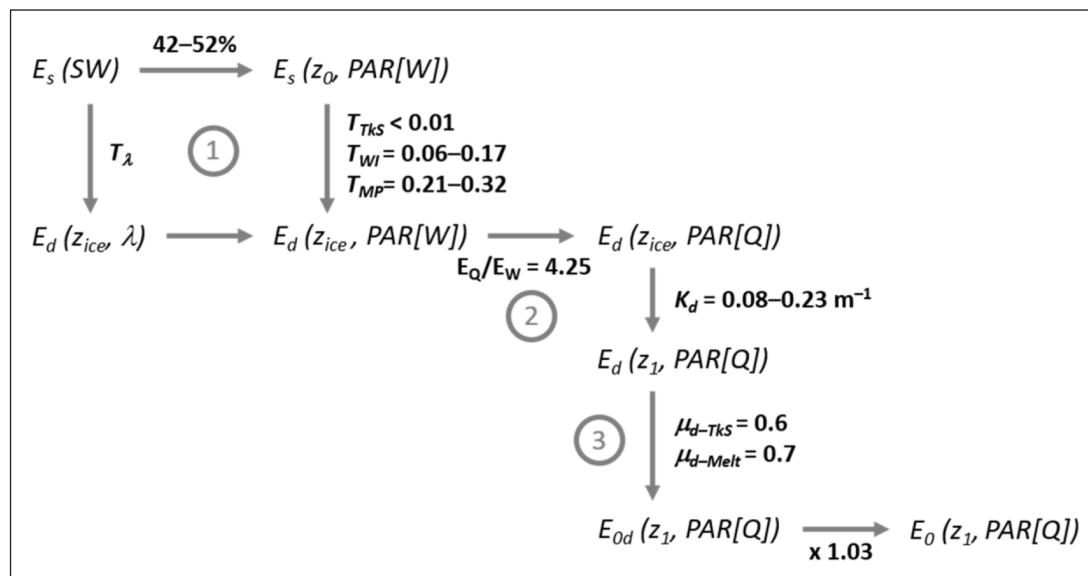


Figure 10: Parametrization of the under-ice light field. Flow chart of attributes to describe the transmittance (T) of incident shortwave (SW) and PAR irradiance through sea ice with a thick snow cover (TkS), white ice (WI) and ponded ice (MP), and the under-ice propagation of PAR: downwelling vertical diffuse attenuation coefficient (K_d), downwelling average cosine (μ_d) and ratio (E_Q/E_W) to convert PAR stated in energy units [W] into photon flux density [Q]. Transmittance and the change in K_d over the sampling period are given as ranges. PAR-fraction of incident shortwave radiation taken from Yu et al. (2015). DOI: <https://doi.org/10.1525/elementa.363.f10>

types. Spectral irradiance measurements were a requirement to derive these coefficients and to convert between units. However, irradiance data in biological studies are often measured using integrated PAR band sensors, in units of quanta, with sometimes little consideration of the prevailing light field (e.g., use of only a planar sensor). The presented results show variations of each coefficient in relation to the prevailing surface conditions to describe the propagation and attenuation of PAR in the water column.

In the next step, these coefficients can be applied in primary production studies as well as in models to calculate PAR availability beneath Arctic landfast sea ice, even if only incident solar irradiance is known. Information about the sea ice surface from drone or satellite imagery can be used to assess the spatial heterogeneity of the surface, so that regional PAR transmittance can be calculated following Equation 3 of bulk transmittance (\bar{T}), first presented by Perovich (2005) and later confirmed in a model exercise of ponded first year sea ice by Taskjelle et al. (2017).

$$\bar{T}(PAR, t) = \bar{T}_s(PAR, t)A_s(t) + \bar{T}_w(PAR, t)A_w(t) + \bar{T}_{MP}(PAR, t)A_{MP}(t) + (1 - \alpha_w(PAR))A_w(t) \quad (3)$$

Average values of PAR transmittance, as presented in this paper, for snow-covered (\bar{T}_s), melt pond-covered (\bar{T}_{MP}) and white ice (\bar{T}_w), their area fraction (A) as well as the surface albedo of water (α_w) can be used to calculate regional PAR transmittance at a given time (t). The subsequently gained, still planar under-ice PAR values (E_d), together with the average cosine $\mu_d(PAR)$ and vertical diffuse attenuation coefficient $K_d(PAR)$ from **Figure 8**, can now be applied to

estimate vertical profiles of downwelling scalar irradiance (E_d) following Equation 4.

$$E_{0d}(PAR, z_2) = \frac{1}{\mu_d(PAR)} E_d(PAR, z_1) e^{-K_d(PAR)(z_2 - z_1)} \quad (4)$$

4 Conclusion

During melt season, changes in the under-ice light field can occur over a relatively short time period and, in turn, can cause a large error in the measurement of radiation available for photosynthesis. Our investigation aimed to minimize the error by providing new information about coefficients to describe the propagation of transmitted PAR below the sea ice cover in spring. Large variation in the apparent optical properties were shown over time and water depth due to a decreased surface albedo with the melting of snow and the appearance of melt ponds as well as an increase in scattering and absorption processes in the water column. The presented measurements of the downwelling average cosine are the first reported beneath sea ice and are in good agreement with modelled values. Significant differences in $\mu_d(PAR)$ were observed directly beneath the ice bottom, but not with increasing depth. Hence, error in the calculation of under-ice primary production can be avoided if measured downwelling irradiance is converted into scalar irradiance by using an average cosine of 0.7 (0.6 beneath snow-covered sea ice).

For future statements about the timing of primary production beneath the thinning Arctic ice pack, more information is still needed on the evolution of the angular distribution of the underwater light field over a diurnal cycle. With continuing melt progression, low sun angles, longer daylight and refreezing of the melting sea ice

surface caused by low night temperatures are likely to have a strong impact on the transmission and angular distribution of the radiant flux penetrating the ice-covered ocean. Here, the use of Monte-Carlo simulations to create a 3D model of the average cosine will be beneficial to characterize the heterogeneous light climate in spring.

Data Accessibility Statement

All data are accessible at the Green Edge database (<http://www.obs-vlfr.fr/proof/php/GREENEDGE/greenedge.php>).

Supplemental files

The supplemental files for this article can be found as follows:

- **Figure S1.** Planar transmittance (PAR) profiles at selected wavelengths. DOI: <https://doi.org/10.1525/elementa.363.s1>
- **Figure S2.** Vertical profiles of downwelling PAR. DOI: <https://doi.org/10.1525/elementa.363.s2>
- **Table S1.** Diffuse attenuation coefficient of downwelling PAR (K_d) and scalar PAR (K_p) obtained beneath snow-covered landfast sea ice in 2015. DOI: <https://doi.org/10.1525/elementa.363.s3>
- **Table S2.** Diffuse attenuation coefficient of downwelling PAR (K_d) and scalar PAR (K_p) obtained beneath melting landfast sea ice in 2016. DOI: <https://doi.org/10.1525/elementa.363.s4>

Acknowledgements

This study is a contribution to the Green Edge project which was conducted under the scientific coordination of the Canada Excellence Research Chair on Remote Sensing of Canada's new Arctic frontier and the CNRS & Université Laval Takuvik Joint International laboratory (UMI3376). We specially thank Robert Hodgson and Jeremy Whitehead for their help during the optical measurements, Virginie Galindo for collecting sea ice surface parameters in 2015 and Joséphine Ras, Céline Dimier and Hervé Claustre for providing the HPLC data. Our field campaign was successful thanks to the contribution of J. Ferland, G. Massé, E. Rehm, D. Christiansen-Stowe and M.-H. Forget from the Takuvik laboratory, F. Pinczon du Sel and E. Brossier from Vagabond. This project would not have been possible without the support of the Hamlet of Qikiqtarjuaq and the members of the community as well as the Inuksuit School and its Principal Jacqueline Arsenault. We also thank Kevin Arrigo and another anonymous reviewer for their valuable input, which significantly improved this manuscript.

Funding information

The Green Edge project is funded by the following French and Canadian programs and agencies: ANR (Contract #111112), CNES (project #131425), IPEV (project #1164), CSA, Fondation Total, ArcticNet, LEFE and the French Arctic Initiative (GreenEdge project). Further funding was provided by the Canadian Space Agency and NSERC Discovery Grants to JKE and CJM and ABOL-CFI to CJM &

JKE. SLG was supported by a postdoctoral fellowship from NSERC.

Competing interests

The authors have no competing interests to declare.

Author contributions

- Contributed to conception and design: LCM, JKE, CJM
- Contributed to acquisition of data: Author and all co-authors
- Contributed to analysis and interpretation of data: LCM, JKE, SLG, CJM
- Drafted and/or revised the article: Author and all co-authors
- Approved the submitted version for publication: Author and all co-authors

References

- Antoine, D, Hooker, S, Bélanger, S, Matsuoka, A and Babin, M. 2013. Apparent optical properties of the Canadian Beaufort Sea—Part 1: Observational overview and water column relationships. *Biogeosciences* **10**(7): 4493–4509. DOI: <https://doi.org/10.5194/bg-10-4493-2013>
- Arrigo, KR, Perovich, DK, Pickart, RS, Brown, ZW, van Dijken, GL, Lowry, KE, Mills, MM, Palmer, MA, Balch, WM and Bates, NR. 2014. Phytoplankton blooms beneath the sea ice in the Chukchi Sea. *Deep Sea Res Part II Top Stud Oceanogr* **105**: 1–16. DOI: <https://doi.org/10.1016/j.dsr2.2014.03.018>
- Arrigo, KR, Sullivan, CW and Kremer, JN. 1991. A bio-optical model of Antarctic sea ice. *J Geophys Res Oceans* **96**(C6): 10581–10592. DOI: <https://doi.org/10.1029/91JC00455>
- Bannister, TT. 1992. Model of the mean cosine of underwater radiance and estimation of underwater scalar irradiance. *Limnol Oceanogr* **37**(4): 773–780. DOI: <https://doi.org/10.4319/lo.1992.37.4.0773>
- Barber, DG, Hop, H, Mundy, CJ, Else, B, Dmitrenko, IA, Tremblay, J-E, Ehn, JK, Assmy, P, Daase, M and Candlish, LM. 2015. Selected physical, biological and biogeochemical implications of a rapidly changing Arctic Marginal Ice Zone. *Prog Oceanogr* **139**: 122–150. DOI: <https://doi.org/10.1016/j.pocean.2015.09.003>
- Berwald, JM. 1999. The relationship between the average cosine of the underwater light field and the inherent optical properties of the ocean., in press.
- Berwald, JM, Stramski, D, Mobley, CD and Kiefer, AD. 1995. Influences of absorption and scattering on vertical changes in the average cosine of the underwater light field. *Limnol Oceanogr* **40**(8): 1347–1357. DOI: <https://doi.org/10.4319/lo.1995.40.8.1347>
- Ehn, JK and Mundy, CJ. 2013. Assessment of light absorption within highly scattering bottom sea ice from under-ice light measurements: Implications for Arctic ice algae primary production. *Limnol Oceanogr* **58**(3): 893–902. DOI: <https://doi.org/10.4319/lo.2013.58.3.0893>

- Ehn, JK, Mundy, CJ, Barber, DG, Hop, H, Rossnagel, A and Stewart, J.** 2011. Impact of horizontal spreading on light propagation in melt pond covered seasonal sea ice in the Canadian Arctic. *J Geophys Res Oceans* **116**(C9). DOI: <https://doi.org/10.1029/2010JC006908>
- Frey, KE, Perovich, DK and Light, B.** 2011. The spatial distribution of solar radiation under a melting Arctic sea ice cover. *Geophys Res Lett* **38**(22). DOI: <https://doi.org/10.1029/2011GL049421>
- Galindo, V, Gosselin, M, Lavaud, J, Mundy, CJ, Else, B, Ehn, J, Babin, M and Rysgaard, S.** 2017. Pigment composition and photoprotection of Arctic sea ice algae during spring. *Mar Ecol Prog Ser* **585**: 49–69. DOI: <https://doi.org/10.3354/meps12398>
- Katlein, C, Arndt, S, Nicolaus, M, Perovich, DK, Jakuba, MV, Suman, S, Elliott, S, Whitcomb, LL, McFarland, CJ and Gerdes, R.** 2015. Influence of ice thickness and surface properties on light transmission through Arctic sea ice. *J Geophys Res Oceans* **120**(9): 5932–5944. DOI: <https://doi.org/10.1002/2015JC010914>
- Katlein, C, Nicolaus, M and Petrich, C.** 2014. The anisotropic scattering coefficient of sea ice. *J Geophys Res Oceans* **119**(2): 842–855. DOI: <https://doi.org/10.1002/2013JC009502>
- Katlein, C, Perovich, DK and Nicolaus, M.** 2016. Geometric Effects of an Inhomogeneous Sea Ice Cover on the under Ice Light Field. *Front Earth Sci* **4**: 6. DOI: <https://doi.org/10.3389/feart.2016.00006>
- Kirk, JTO.** 1981. Monte Carlo study of the nature of the underwater light field in, and the relationships between optical properties of, turbid yellow waters. *Mar Freshw Res* **32**(4): 517–532. DOI: <https://doi.org/10.1071/MF9810517>
- Kirk, JTO.** 2011. *Light and Photosynthesis in Aquatic Ecosystems*. Cambridge Univ Pr: New York. DOI: <https://doi.org/10.1017/CBO9781139168212>
- Leppäranta, M, Reinart, A, Erm, A, Arst, H, Hussainov, M and Sipelgas, L.** 2003. Investigation of ice and water properties and under-ice light fields in fresh and brackish water bodies. *Hydrol Res* **34**(3): 245–266. DOI: <https://doi.org/10.2166/nh.2003.0006>
- Light, B, Grenfell, TC and Perovich, DK.** 2008. Transmission and absorption of solar radiation by Arctic sea ice during the melt season. *J Geophys Res Oceans* **113**(C3). DOI: <https://doi.org/10.1029/2006JC003977>
- Light, B, Perovich, DK, Webster, MA, Polashenski, C and Dadic, R.** 2015. Optical properties of melting first-year Arctic sea ice. *J Geophys Res Oceans* **120**(11): 7657–7675. DOI: <https://doi.org/10.1002/2015JC011163>
- Massicotte, P, Bécu, G, Lambert-Girard, S, Leymarie, E and Babin, M.** 2018. Estimating Underwater Light Regime under Spatially Heterogeneous Sea Ice in the Arctic. *Appl Sci* **8**(12): 2693. DOI: <https://doi.org/10.3390/app8122693>
- Mobley, CD.** 1994. *Light and Water: Radiative Transfer in Natural Waters*. Academic press.
- Morel, A.** 1978. Available, usable, and stored radiant energy in relation to marine photosynthesis. *Deep Sea Res* **25**(8): 673–688. DOI: [https://doi.org/10.1016/0146-6291\(78\)90623-9](https://doi.org/10.1016/0146-6291(78)90623-9)
- Morel, A.** 1991. Light and marine photosynthesis: a spectral model with geochemical and climatological implications. *Prog Oceanogr* **26**(3): 263–306. DOI: [https://doi.org/10.1016/0079-6611\(91\)90004-6](https://doi.org/10.1016/0079-6611(91)90004-6)
- Morel, A and Gentili, B.** 2004. Radiation transport within oceanic (case 1) water. *J Geophys Res Oceans* **109**(C6). DOI: <https://doi.org/10.1029/2003JC002259>
- Morel, A and Smith, RC.** 1974. Relation between total quanta and total energy for aquatic photosynthesis. *Limnol Oceanogr* **19**(4): 591–600. DOI: <https://doi.org/10.4319/lo.1974.19.4.0591>
- Mundy, CJ, Gosselin, M, Gratton, Y, Brown, K, Galindo, V, Campbell, K, Levasseur, M, Barber, D, Papakyriakou, T and Bélanger, S.** 2014. Role of environmental factors on phytoplankton bloom initiation under landfast sea ice in Resolute Passage, Canada. *Mar Ecol Prog Ser* **497**: 39–49. DOI: <https://doi.org/10.3354/meps10587>
- Nicolaus, M and Katlein, C.** 2013. Mapping radiation transfer through sea ice using a remotely operated vehicle (ROV). *The Cryosphere* **7**(3): 763. DOI: <https://doi.org/10.5194/tc-7-763-2013>
- Nicolaus, M, Katlein, C, Maslanik, J and Hendricks, S.** 2012. Changes in Arctic sea ice result in increasing light transmittance and absorption. *Geophys Res Lett* **39**(24). DOI: <https://doi.org/10.1029/2012GL053738>
- Oziel, L, Massicotte, P, Randelhoff, A, Vladoiu, A, Lacour, L, Lambert-Girard, S, Dumont, D, Cuypers, Y, Bouruet-Aubertot, P and Babin, M.** n.d. Seasonal dynamic of environmental factors influencing under-ice spring bloom in the Baffin Bay. *Elementa*, in press.
- Pavlov, AK, Taskjelle, T, Kauko, HM, Hamre, B, Stephen, HR, Assmy, P, Duarte, P, Fernández-Méndez, M, Mundy, CJ and Granskog, MA.** 2017. Altered inherent optical properties and estimates of the underwater light field during an Arctic under-ice bloom of *Phaeocystis pouchetii*. *J Geophys Res Oceans* **122**(6): 4939–4961. DOI: <https://doi.org/10.1002/2016JC012471>
- Perovich, DK.** 1996. The Optical Properties of Sea Ice. *DTIC Document*.
- Perovich, DK.** 2005. On the aggregate-scale partitioning of solar radiation in Arctic sea ice during the Surface Heat Budget of the Arctic Ocean (SHEBA) field experiment. *J Geophys Res Oceans* **110**(C3). DOI: <https://doi.org/10.1029/2004JC002512>
- Platt, T, Gallegos, C and Harrison, W.** 1980. Photoinhibition of photosynthesis in natural assemblages of marine phytoplankton. *J Mar Res* **38**: 687–701.
- Ras, J, Claustre, H and Uitz, J.** 2008. Spatial variability of phytoplankton pigment distributions in the Subtropical South Pacific Ocean: comparison between in situ

- and predicted data. *Biogeosciences* **5**(2): 353–369. DOI: <https://doi.org/10.5194/bg-5-353-2008>
- Reinart, A, Arst, H, Blanco-Sequeiros, A and Herlevi, A.** 1998. Relation between underwater irradiance and quantum irradiance in dependence on water transparency at different depths in the water bodies. *J Geophys Res Oceans* **103**(C4): 7749–7752. DOI: <https://doi.org/10.1029/97JC03645>
- Sathyendranath, S, Platt, T, Caverhill, CM, Warnock, RE and Lewis, MR.** 1989. Remote sensing of oceanic primary production: computations using a spectral model. *Deep Sea Res Part Oceanogr Res Pap* **36**(3): 431–453. DOI: [https://doi.org/10.1016/0198-0149\(89\)90046-0](https://doi.org/10.1016/0198-0149(89)90046-0)
- Taskjelle, T, Hudson, SR, Granskog, MA and Hamre, B.** 2017. Modelling radiative transfer through ponded first-year Arctic sea ice with a plane-parallel model. *The Cryosphere* **11**(5): 2137–2148. DOI: <https://doi.org/10.5194/tc-11-2137-2017>
- Voss, KJ.** 1989. Use of the radiance distribution to measure the optical absorption coefficient in the ocean. *Limnol Oceanogr* **34**(8): 1614–1622. DOI: <https://doi.org/10.4319/lo.1989.34.8.1614>
- Yu, X, Wu, Z, Jiang, W and Guo, X.** 2015. Predicting daily photosynthetically active radiation from global solar radiation in the Contiguous United States. *Energy Convers Manag* **89**: 71–82. DOI: <https://doi.org/10.1016/j.enconman.2014.09.038>

How to cite this article: Matthes, LC, Ehn, JK, L.-Girard, S, Pogorzelec, NM, Babin, M and Mundy, CJ. 2019. Average cosine coefficient and spectral distribution of the light field under sea ice: Implications for primary production. *Elem Sci Anth*, 7: 25. DOI: <https://doi.org/10.1525/elementa.363>

Domain Editor-in-Chief: Jody W. Deming, School of Oceanography, University of Washington, US

Associate Editor: Kevin Arrigo, Environmental Earth System Science, Stanford University, US

Knowledge Domain: Ocean Science

Part of an *Elementa* Special Feature: Green Edge

Submitted: 25 November 2018 **Accepted:** 17 May 2019 **Published:** 13 June 2019

Copyright: © 2019 The Author(s). This is an open-access article distributed under the terms of the Creative Commons Attribution 4.0 International License (CC-BY 4.0), which permits unrestricted use, distribution, and reproduction in any medium, provided the original author and source are credited. See <http://creativecommons.org/licenses/by/4.0/>.



Elem Sci Anth is a peer-reviewed open access journal published by University of California Press.

OPEN ACCESS